Chao Xiong | Claudia Stolle | Hermann Lühr | Jaeheung Park | Bela G. Fejer | Guram N. Kervalishvili

Scale analysis of equatorial plasma irregularities derived from Swarm constellation

FULL PAPER

Scale analysis of equatorial plasma irregularities derived from Swarm constellation

Chao Xiong[1]*, Claudia Stolle[1,2], Hermann Lühr[1], Jaeheung Park[3], Bela G. Fejer[4] and Guram N. Kervalishvili[1,5]

Abstract

In this study, we investigated the scale sizes of equatorial plasma irregularities (EPIs) using measurements from the Swarm satellites during its early mission and final constellation phases. We found that with longitudinal separation between Swarm satellites larger than 0.4°, no significant correlation was found any more. This result suggests that EPI structures include plasma density scale sizes less than 44 km in the zonal direction. During the Swarm earlier mission phase, clearly better EPI correlations are obtained in the northern hemisphere, implying more fragmented irregularities in the southern hemisphere where the ambient magnetic field is low. The previously reported inverted-C shell structure of EPIs is generally confirmed by the Swarm observations in the northern hemisphere, but with various tilt angles. From the Swarm spacecrafts with zonal separations of about 150 km, we conclude that larger zonal scale sizes of irregularities exist during the early evening hours (around 1900 LT).

Keywords: Equatorial plasma irregularities, Ionospheric scale lengths, Swarm constellation

Introduction

At the low-latitude ionosphere, the equatorial plasma irregularities (EPIs), also often called equatorial plasma bubbles (EPBs) or equatorial spread-F (ESF), have been a subject of intense research for several decades. Their morphology, including the generation and evolution processes, spatial structures, global distribution, as well as their effects on the global navigation satellite system (GNSS) have widely been investigated by ground-based radars and in situ satellite observations (Tsunoda 1980; Huang et al. 2001; Burke et al. 2004; Kil et al. 2004; Su et al. 2006; Stolle et al. 2006; Yokoyama et al. 2007; Xiong et al. 2010, 2012; Huang et al. 2014; Park et al. 2015a). These plasma irregularities usually cover a range of scale sizes, from thousands of kilometers to a few meters (e.g., Zargham and Seyler 1989; Hysell and Seyler 1998). EPIs with scale sizes larger than about 100 km, between 10 and 100 m, and smaller than 100 m have been classified as large-, intermediate-, and small-scale structures, respectively (Lühr et al. 2014).

Singh et al. (1997) presented some examples of EPIs from the Atmosphere Explorer E (AE-E) satellite observations showing that EPIs can develop from wavy density structures in the bottom side F-layer around sunset. These wavy structures with zonal (east–west) wavelengths of about 150–880 km evolved later into either large-scale depletions or multiple depleted patches. In a fully developed EPI event, structures with wavelengths from 690 km down to about 0.5 km were simultaneously present. Plasma density measurements with high sampling rates (up to 1024 Hz) on board the ROCSAT-1 satellite have provided a comprehensive view of the spectral characteristics of EPIs (Su et al. 2001). They also showed that the plasma irregularity spectrum can be approximated by a power law with piecewise constant spectral indices. In the meridional (north–south) direction, the 50-Hz magnetic field data from the CHAMP satellite revealed EPI structures with scale size as small as 50 m (Stolle et al. 2006).

In situ satellite measurements mainly detect EPI structures along the satellite track. For a single spacecraft mission, the plasma irregularities can only be sampled either in the zonal direction (for low-inclination satellites, such as AE-E, ROCSAT-1, and C/NOFS) or in the meridional direction (for near-polar orbiting satellites, such

*Correspondence: bear@gfz-potsdam.de
[1] GFZ German Research Centre for Geosciences, Telegrafenberg, 14473 Potsdam, Germany
Full list of author information is available at the end of the article

Xiong *et al. Earth, Planets and Space* (2016) 68:121

Page 2 of 12

as CHAMP and GRACE). ESA's newly launched Swarm constellation comprised of three spacecrafts (with the lower pair flying side-by-side) providing now the opportunity for investigating EPIs in both meridional and zonal directions. Related case studies from Swarm observations focusing on a dayside plasma depletion (Park et al. 2015b) and its relation to GNSS signal losses (Buchert et al. 2015) have already been reported.

In this paper, we present a statistical study of EPI scale sizes, as derived from the Swarm constellation measurements. We aim to reveal the typical scale sizes of EPIs in both the meridional and zonal directions. In the section to follow, we first introduce the data set. Examples and statistical results of EPIs are presented in section "Results." In section "Discussion and summary," we will discuss our observations in the context of earlier reports and summarize our findings.

Data set and processing approach
Data set
The Swarm fleet, comprising three spacecrafts, was launched on November 22, 2013, into a near-polar (87.5° inclination) orbit with initial altitude of about 500 km. From January 2014 onward, the three spacecrafts were maneuvered apart and achieved their final constellation on April 17, 2014. From then on, the lower pair, Swarm A and C, are flying side-by-side at an altitude of about 470 km, separated by about 1.4° in longitude. The third spacecraft, Swarm B, orbits the Earth at about 520 km with a somewhat higher inclination. The plasma density data set measured by the electric field instrument (EFI) onboard Swarm is available at http://earth.esa.int/swarm, including the Langmuir probe (LP)-derived plasma density data with a time resolution of 2 Hz.

Processing approach
We focus on observations from Swarm satellites during two periods: the early mission phase and the final constellation phase. Figure 1 presents the evolution of the longitudinal separation and time lag between Swarm spacecrafts when they pass the geographic equator during both periods. The data used for the early mission phase are from December 09, 2013 to January 22, 2014. Then, the three spacecrafts flew approximately in a string of pearls configuration at almost the same altitude (about 500 km), and Swarm B, the leading spacecraft, was closer to Swarm A than to Swarm C. The three spacecrafts were divided into three pairs and presented with different colors as shown in Fig. 1a, b. We see that the longitudinal separations between the spacecrafts gradually increased for all three pairs. Take Swarm B/A for example, their longitudinal separation increased from 0.1° to 0.4°. During the first period, the local times (LT) covered by the three

spacecrafts were almost the same, which decreased from 0100 to 2100 LT for the descending node, as indicated by the gray dashed line. As shown in Fig. 1b, the time lag (in seconds, corresponding to the latitudinal separation) between the spacecrafts increased simultaneously with their longitudinal separation (ΔGlon, in degree), roughly as the same linear function for all three pairs:
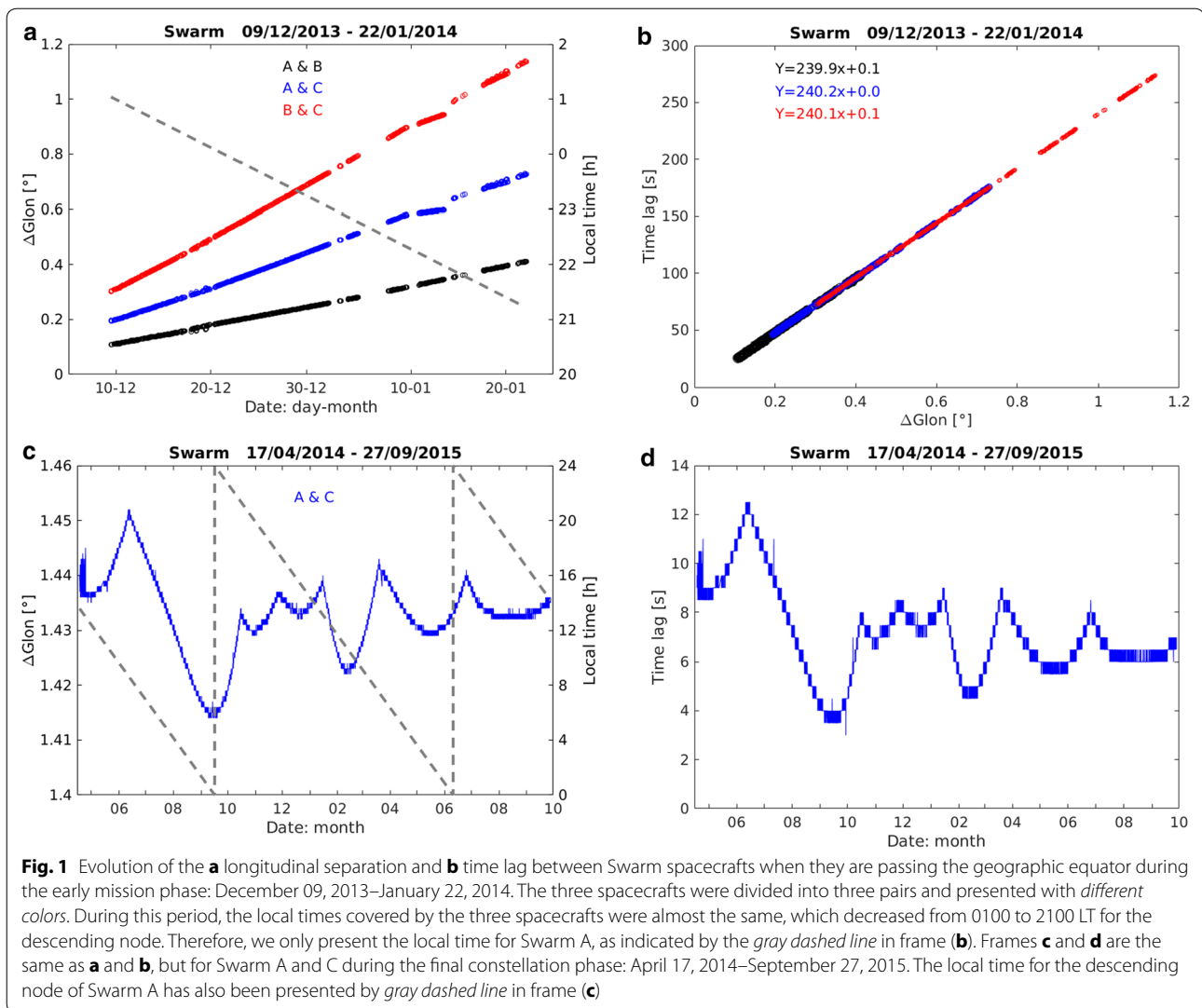
$$\text{Time lag} = 240 \cdot \Delta\text{Glon} \tag{1}$$

At the end of the first period, the time lag increased to about 1.6 min, 3 min, and 5 min between Swarm B/A, A/C, and B/C, respectively.

After the final constellation has been completed on April 17, 2014, Swarm A and C started flying side-by-side at an altitude of about 470 km, separated by about 1.4° in longitude, with Swarm C a few seconds ahead of Swarm A. The evolutions of their longitudinal and temporal separations are presented in Fig. 1c, d. For the second period, we used data from April 17, 2014 to September 27, 2015, and consider only observations from the lower spacecraft pair, Swarm C/A.
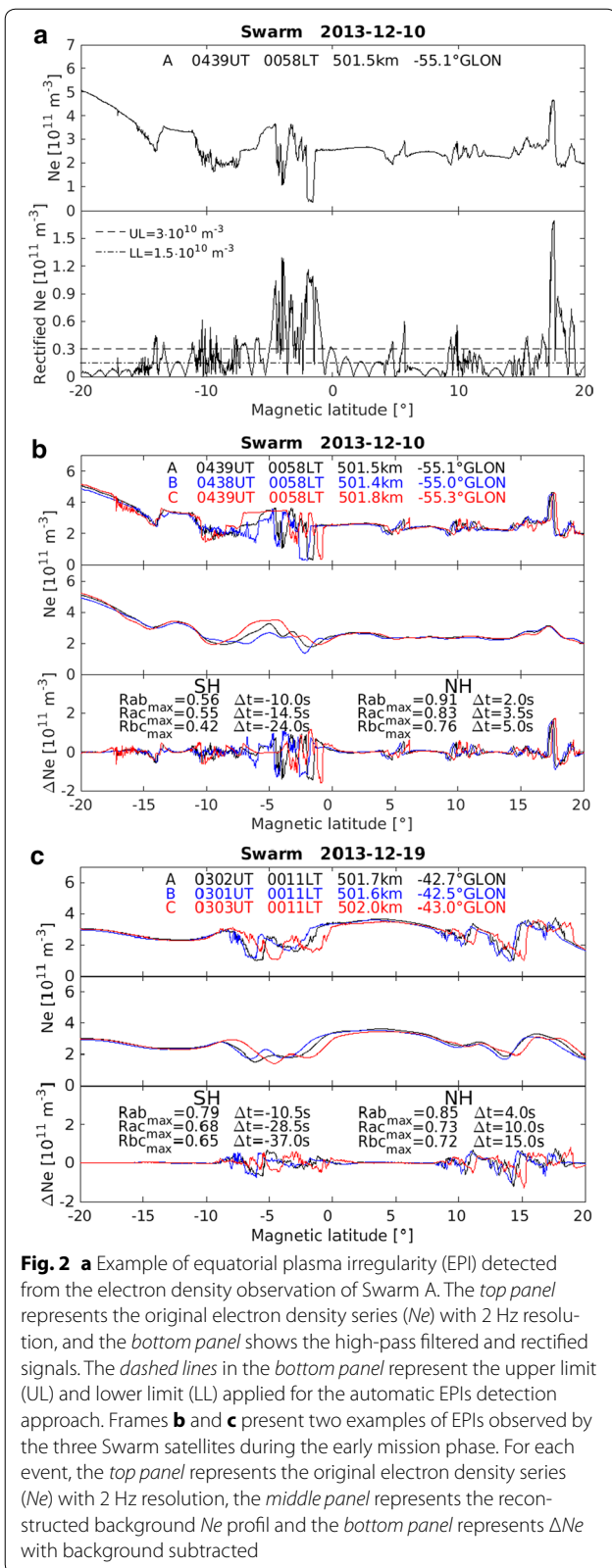
For detecting EPI events from the Swarm electron density measurements, we used the same approach as described by (Xiong et al. 2010). Electron density (*Ne*) time series from each equatorial orbital segment (within ±40° magnetic latitude, MLAT) are first high-pass filtered with a cutoff period of 40 s, corresponding to an along-track wavelength of about 300 km. The magnetic latitude we used is calculated by the Apex or Quasi-Dipole magnetic field model, which has been defined by Richmond (1995) and updated by Emmert et al. (2010). Subsequently, the filtered signal is rectified. Values exceeding an upper limit (UL) are identified as an EPI event. For each event, the rectified signal should have multi-peaked values above UL, and this event is limited along the orbit, by rectified signals below a lower limit (LL) for at least 3° north and south of the event. Otherwise, the fluctuations of rectified signal are attributed to enhanced noise and are considered as not significant. The thresholds of UL and LL are set here to 3×10^{10} m^{-3} and 1.5×10^{10} m^{-3}, respectively, which are mainly estimated from the level of quiet-time *Ne* variations at Swarm altitudes. Using such a method for detecting plasma irregularities, we focus on EPIs with plasma structures scale lengths less than 300 km.

Figure 2a presents such an EPI example observed by Swarm A on December 10, 2013, and the dashed lines in the bottom panel indicate the thresholds of UL and LL. Then the EPI events during both periods were identified by an automated procedure as described above and have later been checked visually. Data from magnetically disturbed periods (*Kp* > 3.5) have been excluded to reduce possible storm-related effects.

Xiong *et al. Earth, Planets and Space* (2016) 68:121

Page 3 of 12

Fig. 1 Evolution of the **a** longitudinal separation and **b** time lag between Swarm spacecrafts when they are passing the geographic equator during the early mission phase: December 09, 2013–January 22, 2014. The three spacecrafts were divided into three pairs and presented with *different colors*. During this period, the local times covered by the three spacecrafts were almost the same, which decreased from 0100 to 2100 LT for the descending node. Therefore, we only present the local time for Swarm A, as indicated by the *gray dashed line* in frame (**b**). Frames **c** and **d** are the same as **a** and **b**, but for Swarm A and C during the final constellation phase: April 17, 2014–September 27, 2015. The local time for the descending node of Swarm A has also been presented by *gray dashed line* in frame (**c**)

For deriving EPI scale sizes, we determine their correlation from the electron density recordings between two Swarm spacecrafts. For the early mission phase, we divided the spacecraft into three pairs: Swarm B/A, A/C and B/C. As we are interested in plasma irregularities, the background density of each EPI event has been subtracted to reduce the effect of non-depleted variations on the correlation analysis. For each equatorial orbital segment with EPI, the Ne time series with 2 Hz resolution were first projected onto MLAT, then a multi-wavelet method has been applied to the MLAT profile of Ne. The wavelet function we used is "coiflets," which is discrete, near symmetric and has scaling functions with vanishing moments (Beylkin et al. 1991). The wavelet coefficients with wavelengths between 240 and 960 km were used to reconstruct the background Ne profile. As reported in previous studies, EPIs exhibit inverted-C shell structures when projected onto the horizontal

plane. In case of a westward-tilted inverted-C shell structure, more poleward EPI parts appear further westward (Kelley et al. 2003; Kil et al. 2004; Huba et al. 2009; Park et al. 2015a). This means that the Swarm spacecraft on the westside is expected to observe depletions at higher latitude than the spacecraft on the eastside. We examined such expected feature further by using a cross-correlation analysis. We treated separately the data from the two hemispheric parts (0° to ±20° MLAT). For each hemisphere, the electron density recording of the eastside spacecraft was taken as reference and the other one was time-shifted from −100 to 100 s. The maximum value of the correlation coefficients (R_{max}) and the corresponding time shifts (Δt) were recorded for following statistical analysis. To keep consistency, a positive value of Δt means that the electron density from the westside spacecraft had to be shifted equatorward to get R_{max} in both hemispheres.

Xiong *et al. Earth, Planets and Space* (2016) 68:121

Page 4 of 12

Fig. 2 a Example of equatorial plasma irregularity (EPI) detected from the electron density observation of Swarm A. The *top panel* represents the original electron density series (*Ne*) with 2 Hz resolution, and the *bottom panel* shows the high-pass filtered and rectified signals. The *dashed lines* in the *bottom panel* represent the upper limit (UL) and lower limit (LL) applied for the automatic EPIs detection approach. Frames **b** and **c** present two examples of EPIs observed by the three Swarm satellites during the early mission phase. For each event, the *top panel* represents the original electron density series (*Ne*) with 2 Hz resolution, the *middle panel* represents the reconstructed background *Ne* profil and the *bottom panel* represents Δ*Ne* with background subtracted

Results

Examples of EPIs observed by Swarm

Figure 2b, c presents two examples of EPIs observed by Swarm during the first study period. For both events, the top panel presents the latitudinal profiles of the original electron density time series (*Ne*, 2 Hz resolution) with different colors for different spacecrafts. The epochs, altitudes and longitudes when the spacecraft passed the geographic equator are listed in the topside. The middle panel shows the reconstructed background *Ne* and the bottom panel presents Δ*Ne* with background variations subtracted. For the first event observed on December 10, 2013, the three spacecrafts flew at an altitude of about 501 km. Swarm B was the leading spacecraft, crossing the geographic equator 1 min earlier than A and C. In this case, Swarm A was 0.1° (about 11 km) westward of B and 0.2° (about 22 km) eastward of C, respectively. As the three spacecrafts were so close in time and space, they observed similar plasma density irregularities in both hemispheres. In the northern hemisphere, the correlations of the density depletions, R_{max}, attained values of 0.91, 0.83 and 0.76 for the pairs Swarm B/A, A/C and B/C, respectively. As Swarm B/A were most closely spaced, R_{max} is largest, as expected. Furthermore, a correlation less than 1.0 between Swarm B/A also reveals that the EPI had fine structure with zonal extent less than 0.1° (about 11 km) or that the plasma density structure did change within the 27 s leading time between Swarm B/A. As described in section "Processing approach," to calculate the correlations, for each Swarm pair, we took the Δ*Ne* series from the eastside spacecraft as reference and time-shifted the other one. In the northern hemisphere, we found Δ*t* is about 2.0, 3.5 and 5.0 s for the three pairs, respectively. The positive values of Δ*t* result from the EPI inverted-C shell structure. In fact, from the latitudinal profiles of electron density, we can also see that Swarm C observed the density depletion at highest latitudes, as expected for the most westerly spacecraft.

However, the correlations are significantly reduced in the southern hemisphere with R_{max} of 0.56, 0.55 and 0.42 for the three pairs, compared to the northern hemisphere. The corresponding Δ*t* with values of −10.0, −14.5 and −24.0 s are also somewhat larger in absolute value than those in the northern hemisphere. And we found the electron density latitudinal profiles show much finer structures between 6° and 12°S MLAT, which might contribute to the lower correlations in the southern hemisphere. In addition, the negative values of Δ*t* in the southern hemisphere seem not support the westward-tilted inverted-C shell structure of EPI.

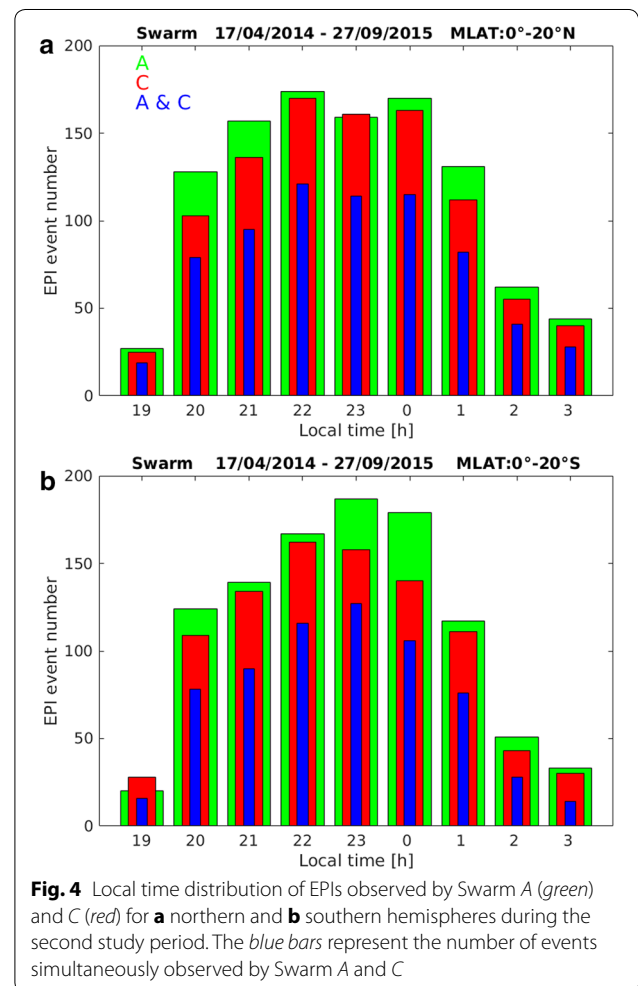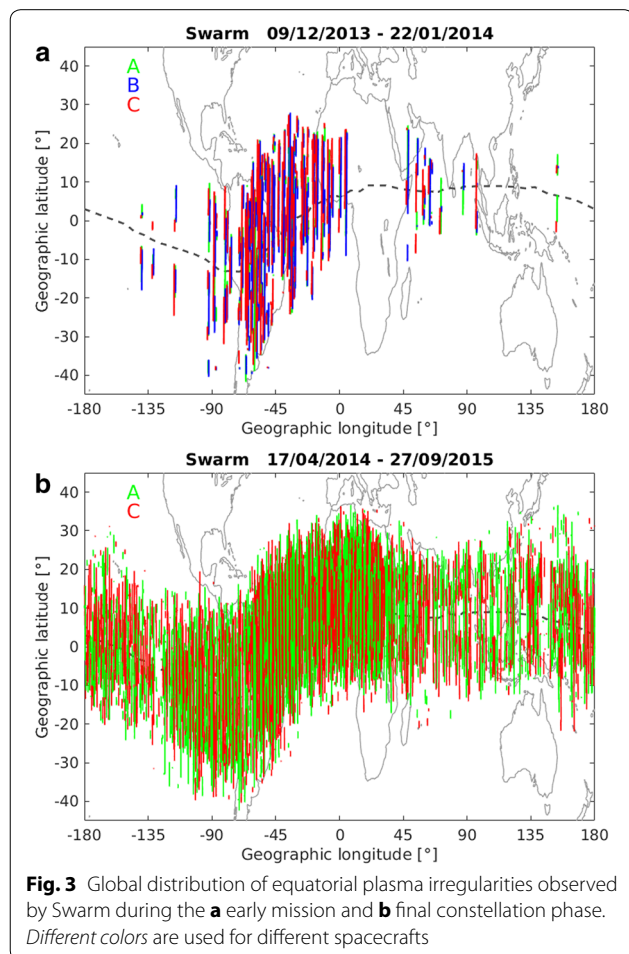Xiong *et al. Earth, Planets and Space* (2016) 68:121

Page 5 of 12

Figure 2c presents another example of EPI on December 19, 2013. The electron densities measured by Swarm also show similar depletions in both hemispheres. In this case, the three spacecrafts were practically at the same altitude of about 501 km, and Swarm B was 1 and 2 min ahead of Swarm A and C, respectively. The longitudinal separation between Swarm B/A increased to 0.2° (about 22 km), and 0.3° (about 33 km) between Swarm A/C. In the northern hemisphere, R_{max} was larger than 0.7 for all the three pairs and again was largest for Swarm B/A. In the southern hemisphere, R_{max} is somewhat smaller but still around 0.7. The time shifts (Δt) were again mainly positive in the northern and negative in the southern hemisphere.

Statistic results

With the approach described above, there were about 60 EPI events detected by all the three spacecrafts during the first period and about 1000 events detected by Swarm A and C during the second period. Figure 3 shows the global distribution of the equatorial plasma irregularities

for both periods. During the first period, most of the plasma irregularities occurred in the longitude sector between −90 and 0°E, which reflects well the seasonal dependence of EPI's occurrence almost exclusively above the south American/Atlantic sector during December solstice months (e.g., Stolle et al. 2008). During the time of the final constellation phase considered in this study, the EPIs were more evenly distributed in longitude; however, the increased concurrency between longitude −90° and 0°E is again visible.

The longitudinal separation and local time of sampling varied simultaneously during the first period. Therefore, it is difficult to separate their effects on EPIs from the data during this period. Conversely, the longitudinal separation between Swarm A and C was almost fixed (about 1.4° in longitude) during the second period, which allowed us to check for a possible local time dependence on EPI scale sizes. Figure 4 shows the local time distribution of EPI events observed by Swarm A and C during the second period. The green and red bars indicate EPIs detected by each of the spacecraft A

Fig. 3 Global distribution of equatorial plasma irregularities observed by Swarm during the **a** early mission and **b** final constellation phase. *Different colors* are used for different spacecrafts

Fig. 4 Local time distribution of EPIs observed by Swarm *A* (*green*) and *C* (*red*) for **a** northern and **b** southern hemispheres during the second study period. The *blue bars* represent the number of events simultaneously observed by Swarm *A* and *C*

Xiong *et al. Earth, Planets and Space* (2016) 68:121

Page 6 of 12

and C, respectively. The blue bars represent the number of EPIs simultaneously observed by the two spacecrafts. The number of detections for the individual satellite is always higher than the number when both satellites detect depletions, because the individual satellite may also monitor depletions when the other satellite does not. When comparing the EPI number of detected events between the two satellites, we found EPI occurrence is slightly higher from Swarm A than from Swarm C for almost all local times. Differences in data availability have been excluded, and both satellites provided continuous data sets. Differences in the sensitivity of the instrument can be possible, but we did not explicitly investigate such an effect. Further statistical investigation into the difference in detection is interesting and should be continued with a larger database. However, the occurrence rates of EPIs observed by the two spacecrafts are similar over local time evolution, which increases dramatically between 1900 and 2000 LT and gradually decreases during post-midnight hours.

For statistical analysis of the EPI scale sizes, we calculated $R_{\max}$ and Δt only when EPI was detected by both spacecrafts. Figure 5a, b shows the relation between $R_{\max}$ and Δt in both hemispheres. The circles represent the individual EPI events marked by different colors for the three different pairs. $R_{\max}$ reached larger values when Δt was close to zero, and the focusing is more prominent in the northern hemisphere. Frames c and d present the dependence of $R_{\max}$ on the longitudinal separation ($\Delta Glon$) between the spacecrafts. The gray triangles and vertical lines denote the mean values and the standard deviations for each longitudinal bin (0.1°). The longitudinal separation between spacecrafts varied from 0.1° to 1.2° during this period. A clear trend of the $R_{\max}$ mean values can be found in both hemispheres: R_{max} gradually decreases with $\Delta Glon$ untill $\Delta Glon$ approaches 0.4° (about 44 km). Higher correlations are found for smaller separations, especially in the northern hemisphere. When $\Delta Glon > 0.4°$, the mean values of $R_{\max}$ stay around 0.4 in both hemispheres. The second peak of the $R_{\max}$ mean value at $\Delta Glon = 0.9°$ is possibly caused by the small event number (only three events) within that bin.

We have also calculated the correlations between EPIs but only for those events simultaneously observed by Swarm A and C during the second period. Figure 6a, b shows the relation between $R_{\max}$ and Δt separately for the two hemispheres, with blue circles representing the individual EPI events. Similar to the result during the first study period, we find generally larger $R_{\max}$ when Δt is close to zero. Frames (c) and (d) present the dependence of $R_{\max}$ on local time. The gray triangles and vertical lines are again the mean values and standard deviations for each local time bin (1 h). For given spacecraft longitudinal

separation of about 150 km, $R_{\max}$ shows a considerable spread with a mean value of around 0.4 and standard deviations of ca. 0.2, especially after 2000 LT. These results suggest that the majority of events include plasma density scale sizes less than 150 km. Figure 6e, f shows local time distribution of the occurrence ratio for those EPI events with $R_{\max} > 0.7$ between Swarm A and C. We see clearly that shortly after sunset (around 1900 LT), about 18 % EPIs are found with zonal scale length larger than 150 km ($R_{\max} > 0.7$), and these larger-scale-length EPIs decay fast during later local times.
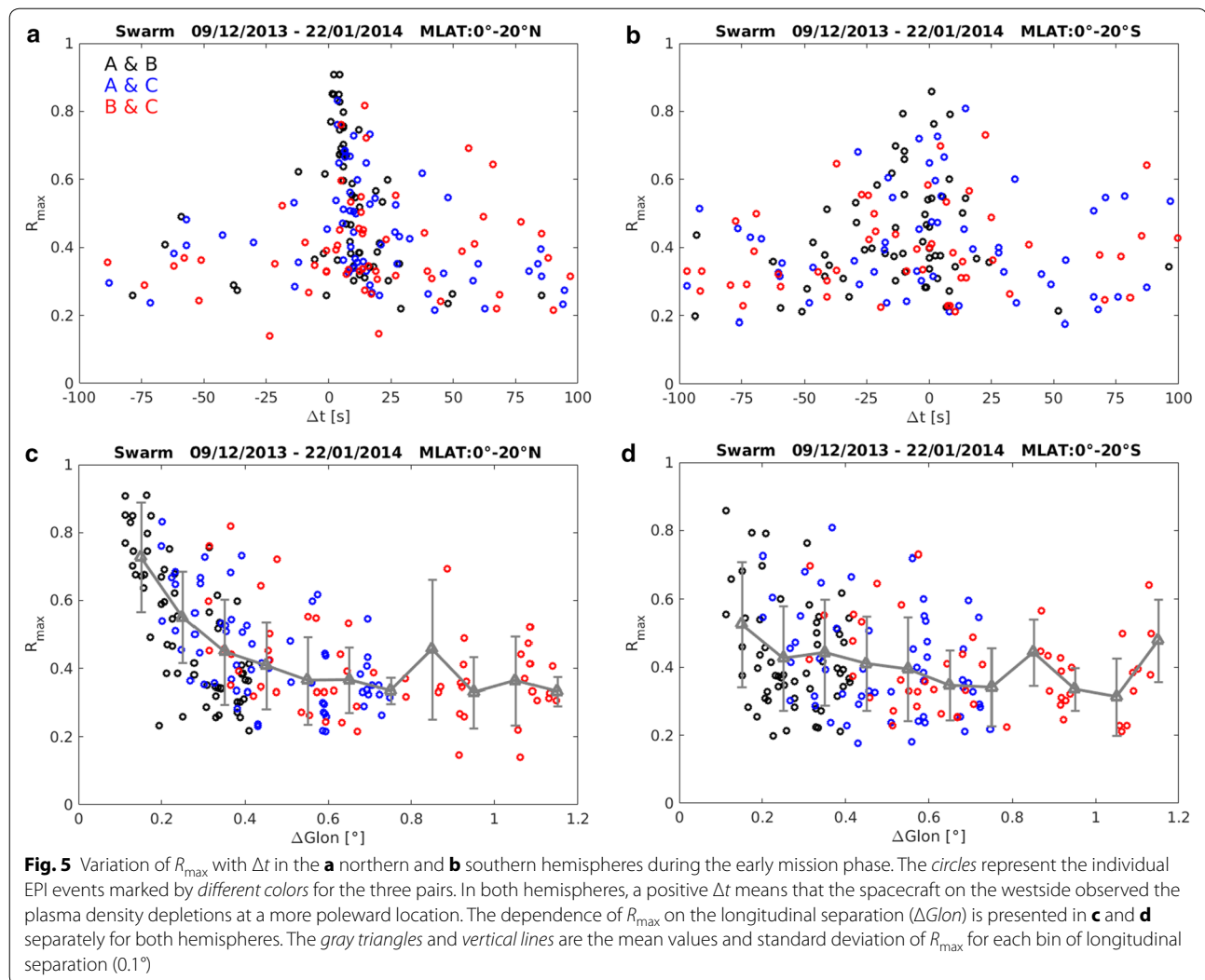
The second study period comprised a data set covering one and a half years, which allowed us for a more detailed investigation of EPIs local time dependence. Since all observations have been made at zonal separation of about 150 km, little correlations are expected between the ΔNe records (2 Hz) of Swarm A and C. We further low-pass-filtered ΔNe with different window sizes (in seconds). One of such example is presented in Fig. 7, which was observed on May 14, 2014. Considering a satellites speed of 7.6 km/s, the filter window sizes of 0.5, 1.5, 2.5, 5, 10, 15 and 20 s correspond to moving-average length about 3.8, 11.4, 19, 38, 76, 114 and 152 km along-track, respectively. At larger moving-average length, the small-scale density irregularities are smoothed out and the $R_{\max}$ values gradually increase. When a 15-s filter was applied, the small-scale plasma irregularities were totally smoothed out, and the $R_{\max}$ values surpassed 0.8 in both hemispheres in this example.

The local time dependence of $R_{\max}$ for different filter window sizes of ΔNe during the second study period is presented in Fig. 8. With larger moving-average lengths, the $R_{\max}$ values gradually increase. When the filter window size increased to 20 s, better correlations ($R_{\max}$ around 0.7) are obtained for all local times. Additionally, relatively larger $R_{\max}$ values are found shortly after sunset, 1900–2000 LT (also seen Fig. 6), which we interpreted as resulting from larger zonal scale sizes during the earlier evening local time as will be discussed in section "Discussion and summary." These scale sizes drop rapidly with local time and are insignificant after 2000 LT.

Discussion and summary

In this study, we analyze the scale sizes of equatorial plasma irregularities based on observations from the Swarm constellation.
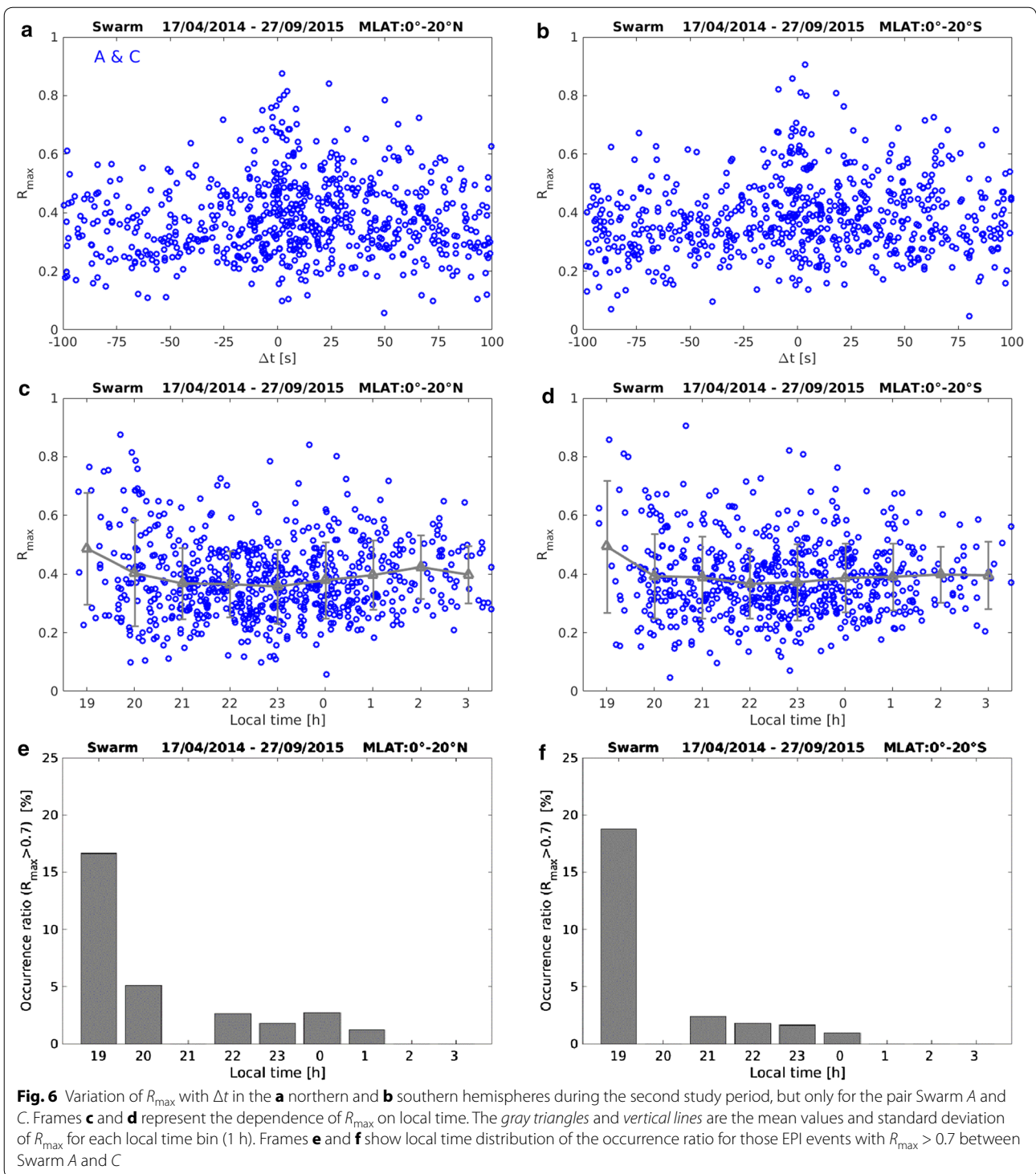
The examples of EPIs presented in Fig. 2 show that the plasma irregularities usually have various scale sizes in the meridional direction, and these structures sometimes are not well correlated in the zonal direction. As shown in Fig. 5, the correlation rapidly decreases between neighboring measurements over tenths of a degree in longitude. With longitudinal separations larger than 0.4°

Xiong *et al. Earth, Planets and Space* (2016) 68:121

Page 7 of 12

Fig. 5 Variation of R_{max} with Δt in the **a** northern and **b** southern hemispheres during the early mission phase. The *circles* represent the individual EPI events marked by *different colors* for the three pairs. In both hemispheres, a positive Δt means that the spacecraft on the westside observed the plasma density depletions at a more poleward location. The dependence of R_{max} on the longitudinal separation ($\Delta Glon$) is presented in **c** and **d** separately for both hemispheres. The *gray triangles* and *vertical lines* are the mean values and standard deviation of R_{max} for each bin of longitudinal separation (0.1°)

(about 44 km), no significant correlation was found any more. This result suggests that small-scale structures within EPIs have short correlation lengths in longitude. Numerical model studies also report typical density depletion diameters of 20–30 km (e.g., Huba and Joyce 2007; Retterer 2010; Yokoyama et al. 2015). Swarm observational results can help to constrain the range of EPIs sizes in simulation studies.

From the two examples presented in Fig. 2, we found Swarm C observed density depletions at highest latitude in the northern hemisphere. Considering the spatial formation of Swarm during the early mission phase (Swarm C is on the most westward), this result is consistent with the positive value of Δt for cross-correlation in the northern hemisphere and supports a westward-tilted inverted-C shell structure of EPIs, which is believed to be present for most of observed irregularity structures. However, the

negative values of Δt in the southern hemisphere seem not to support such a simple model. Huba et al. (2009) showed that the shell structure of EPIs strongly depends on the vertical profile of zonal wind. For different zonal wind conditions, this shell structure can be westward tilted with different angles and sometimes is even eastwardly tilted (see their Fig. 4). Figure 5a, b illustrates this range of variations. In general, for other examples (not shown here), most of the EPI events presented positive Δt in the northern hemisphere (corresponding to westward tilt), but there were also some events of negative Δt in the northern hemisphere with R_{max} larger than 0.6. The Δt in the southern hemisphere is more scattered toward both positive and negative values. For the interpretation of the observed latitude shift, we may have to consider also the magnetic field declination and meridional drifts, and dedicated study may be needed.

Xiong *et al. Earth, Planets and Space* (2016) 68:121

Page 8 of 12

Fig. 6 Variation of R_{max} with Δt in the **a** northern and **b** southern hemispheres during the second study period, but only for the pair Swarm *A* and *C*. Frames **c** and **d** represent the dependence of R_{max} on local time. The *gray triangles* and *vertical lines* are the mean values and standard deviation of R_{max} for each local time bin (1 h). Frames **e** and **f** show local time distribution of the occurrence ratio for those EPI events with $R_{max} > 0.7$ between Swarm *A* and *C*

The R_{max} generally show higher values in the northern hemisphere than in the southern hemisphere during the first study period. This may result from the fact that equatorial plasma irregularities reveal more substructures southern hemisphere. As seen in Fig. 3a,

most of the plasma irregularities during this period were observed in the longitude sector between −90 and 0°E, where the South Atlantic Anomaly (SAA) is located. Figure 9 presents the global distribution of the ambient magnetic field at 500 km derived from the International

Xiong *et al. Earth, Planets and Space* (2016) 68:121

Page 9 of 12

Fig. 7 Example of EPI event observed by Swarm *A* and *C* during the second study period. The panel **a** is the original electron density series (*Ne*) with 2 Hz resolution and **b** is Δ*Ne* with background subtracted. The Δ*Ne* is further filtered with different window size (WS, in seconds), as presented in panels (**c**)–(**h**). Considering a satellite speed of about 7.6 km/s, the filter window sizes of 0.5, 1.5, 2.5, 5, 10, 15 and 20 s correspond to moving-average length of about 3.8, 11.4, 19, 38, 76, 114 and 152 km, respectively

Geomagnetic Reference Field model (IGRF, Thébault et al. 2015). Compared to other longitudes, the magnetic equator at longitudes between −90 and 0°E bends furthest to the geographic southern hemisphere and the difference of the ambient magnetic field between the two hemispheres in this region is the largest compared to other longitudes. The generation of EPIs has often been related to the generalized Rayleigh–Taylor (R–T) theory (Ott 1978; Ossakow 1981; Sultan 1996; Kelley 2009) and can be described with a linear growth rate of:

$$\gamma \approx \frac{\sum_P^F}{\sum_P^F + \sum_P^E} \left[v_z - \frac{g}{v_{in}} \right] \cdot \frac{\nabla n}{n_0} - R \qquad (2)$$

where $\sum_P^F$ and $\sum_P^E$ are the flux tube integrated Pedersen conductivities in the F- and E-region, respectively.

$v_z = E \times \mathbf{B}/B^2$ is the plasma vertical drift related to the ambient magnetic field and zonal electric field E at the magnetic equator. g is the acceleration due to gravitation, v_{in} is the ion-neutral collision frequency, n_0 is the background electron density, ∇n is the electron density gradient and R is the recombination rate. According to this equation, the evolution of EPIs is strongly determined by the strength of the plasma density gradient, but also by the vertical plasma drift that is indirectly proportional to the ambient magnetic field. The low ambient magnetic field between −90 and 0°E in the southern hemisphere is favorable for the evolution of EPIs, and the swift growth of EPIs in this region is expected to develop smaller structures of EPIs. More structured EPIs may be the reason for the relatively lower correlations between the Swarm spacecraft observations in the southern
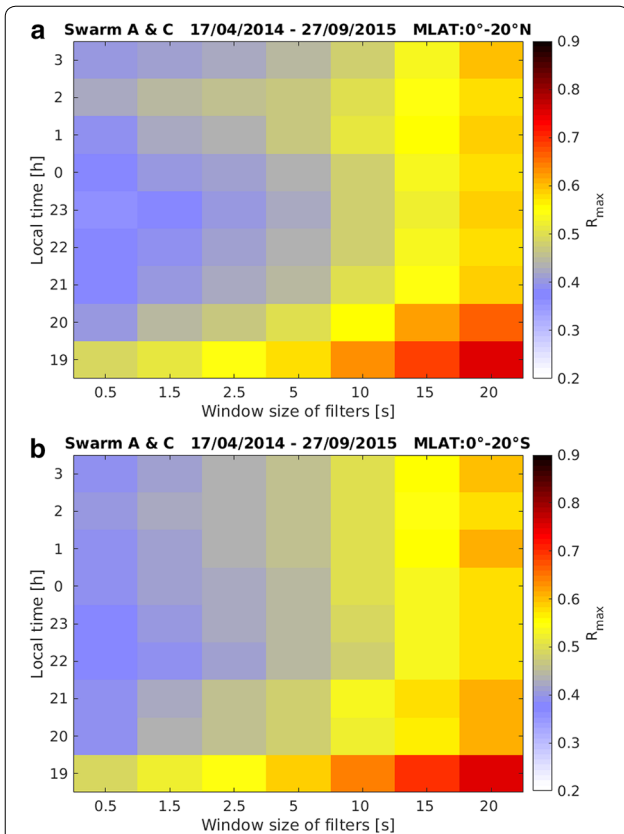
Xiong *et al. Earth, Planets and Space* (2016) 68:121

Page 10 of 12

Fig. 8 R_{max} distribution depending on local time and the filter window sizes of ΔNe in the **a** northern and **b** southern hemispheres during the second study period
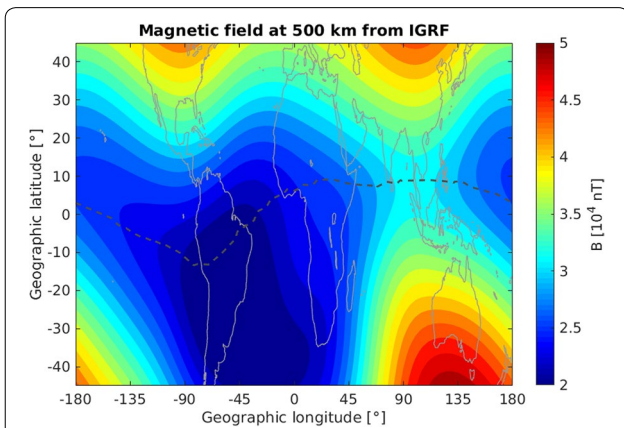

Fig. 9 Global distribution of the ambient magnetic field at 500 km estimated from the IGRF model. The *grey dashed line* indicates the location of the magnetic equator

Another point to be considered here is the southern location of the geomagnetic equator. During December solstice month, being local summer in the southern hemisphere, larger electron densities are expected in the regions south of the geographic equator that has the potential to develop steeper ∇n, and thus enhance the EPI growth rate. We therefore explain the observed lower correlations of EPIs between Swarm A and C in the southern than those in the northern hemisphere by these two effects, low geomagnetic field and southern location of the magnetic equator.

As shown in Figs. 6 and 8, EPIs during the early evening hours show larger correlation values that can be inferred to relatively larger zonal scale size. Figure 10 presents two examples observed by Swarm A and C around 1900 LT during the second study period, which mainly shows wave structures in the density depletion region. These wave structures have large-scale sizes compared to the finer structures of EPIs in the example as shown in Fig. 7, for example. The occurrence of larger zonal scale
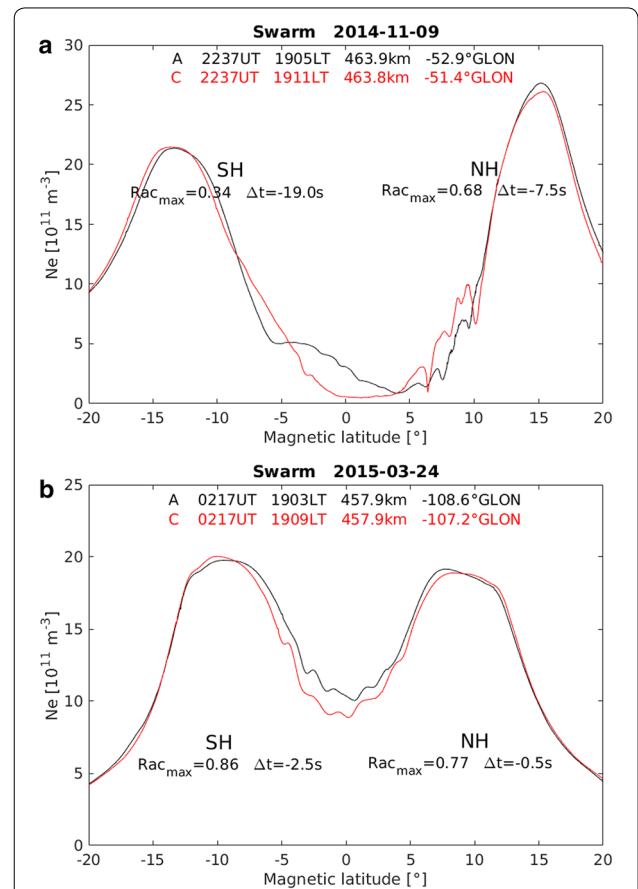
Fig. 10 Two examples **a** on 9 November 2014 and **b** on 24 March 2015 of equatorial plasma irregularities observed by Swarm *A* and *C* during early evening hours (around 1900 LT)

hemisphere. Additionally, the lower ambient magnetic field will slightly enlarge the upward vertical drift, lifting the plasma irregularity to higher altitude, where the ion-neutral frequency, ν_{in}, is lower.

Xiong *et al. Earth, Planets and Space* (2016) 68:121

Page 11 of 12

sizes during early evening hours is consistent with the results reported by Singh et al. (1997) based on measurements from a low-inclination satellite, AE-E. From exploring two orbit examples, these authors suggested that post-sunset plasma irregularities are preceded by wavy structures of up to 540 km wavelengths that broke down to substructures between 1900 LT and 2000 LT. They considered these zonal wave structures shortly after sunset, probably generated by gravity waves, as the initial seed of the plasma density perturbations. Their results also suggested that the sizes of initial wavy structures determine the degree of fragmentation of the resulting depletion structures. Our statistical analyses from the Swarm constellation are in favor to the explanations of Singh et al. (1997). Figure 8 indicates that the zonal scale sizes gradually decrease after 1900 LT, reaching their finest structures around 2100–2300 LT, and slightly increase again during post-midnight hours. A possible relation between the size of early evening structures and the degree of defragmentation of EPIs from the Swarm mission need further investigation that can be expected from a long-term data set of Swarm. Due to its polar orbit, hence its slow local time precessing, initial and resulting structures in the post-sunset F region are, however, not easily detectable by the spacecraft. Joint analyses with observations by ionospheric satellite with inclination of 30° or less will increase significant conclusions in this topic. The US Air Force C/NOFS satellite that operated between April 2008 and November 2015 presently gives such opportunity.

In summary, the Swarm constellation mission provides us with the opportunity to study the scale sizes of equatorial plasma irregularities simultaneously in the meridional and zonal directions. We found that with longitudinal separations between Swarm satellites larger than 0.4° no significant correlation was found any more. This result suggests that EPI structures include plasma density scale sizes less than 44 km in the zonal direction. During the earlier mission period, clearly better correlations of EPIs are obtained in the northern hemisphere, implying more fragmented irregularities in the southern hemisphere where the ambient magnetic field is low. The previously reported inverted-C shell structure of EPIs is generally confirmed by the Swarm observations in the northern hemisphere, but with various tilt angles. From the Swarm spacecraft with zonal separations of about 150 km, we conclude that larger zonal scale sizes of irregularities exist in the early evening hours (around 1900 LT) that are interpreted as larger scale lengths, initial perturbations of post-sunset ionospheric plasma irregularities.

Authors' contributions
CX designed the MATLAB program for finding the equatorial plasma irregularity (EPI) events from Swarm electron density observations, performed the statistical analysis, and drafted the manuscript. CS provided fruitful discussion of the results and drafted the manuscript. HL, JP, BGF, GNK gave constructive suggestions for improving the text. All authors read and approved the final manuscript.

Author details
[1] GFZ German Research Centre for Geosciences, Telegrafenberg, 14473 Potsdam, Germany. [2] Faculty of Science, University of Potsdam, Potsdam, Germany. [3] Korea Astronomy and Space Science Institute, Daejeon, Korea. [4] Center for Atmospheric and Space Science, Utah State University, Logan, UT 84322, USA. [5] M. Nodia Institute of Geophysics, Iv. Javakhishvili Tbilisi State University, Tbilisi, Georgia.

References
Beylkin G, Coifman R, Rokhlin V (1991) Fast wavelet transforms and numerical algorithms. Commun Pure Appl Math 44:141–183

Buchert S, Zangerl F, Sust M, André M, Eriksson A, Wahlund J, Opgenoorth H (2015) SWARM observations of equatorial electron densities and topside GPS track losses. Geophys Res Lett 42:2088–2092. doi:10.1002/2015GL063121

Burke WJ, Gentile LC, Huang CY, Valladares CE, Su SY (2004) Longitudinal variability of equatorial plasma bubbles observed by DMSP and ROCSAT-1. J Geophys Res 109:A12301. doi:10.1029/2004JA010583

Emmert JT, Richmond AD, Drob DP (2010) A computationally compact representation of Magnetic-Apex and Quasi-Dipole coordinates with smooth base vectors. J Geophys Res 115:A08322. doi:10.1029/2010JA015326

Huang CY, Burke WJ, Machuzak JS, Gentile LC, Sultan PJ (2001) DMSP observations of equatorial plasma bubbles in the topside ionosphere near solar maximum. J Geophys Res 106(A5):8131–8142. doi:10.1029/2000JA000319

Huang C-S, de La Beaujardiere O, Roddy PA, Hunton DE, Liu JY, Chen SP (2014) Occurrence probability and amplitude of equatorial ionospheric irregularities associated with plasma bubbles during low and moderate solar activities (2008–2012). J Geophys Res Space Phys 119:1186–1199. doi:10.1002/2013JA019212

Huba JD, Joyce G (2007) Equatorial spread F modeling: multiple bifurcated structures, secondary instabilities, large density 'bite-outs', and supersonic flows. Geophys Res Lett 34:L07105. doi:10.1029/2006GL028519

Huba JD, Ossakow SL, Joyce G, Krall J, England SL (2009) Three-dimensional equatorial spread F modeling: zonal neutral wind effects. Geophys Res Lett 36:L19106. doi:10.1029/2009GL040284

Hysell DL, Seyler CE (1998) A renormalization group approach to estimation of anomalous diffusion in the unstable equatorial F region. J Geophys Res 103(A11):26731–26737. doi:10.1029/98JA02616

Kelley MC (2009) The Earth's ionosphere: electrodynamics and plasma physics, 2nd edn. Elsevier, New York

Kelley MC, Makela JJ, Paxton LJ, Kamalabadi F, Comberiate JM, Kil H (2003) The first coordinated ground- and space-based optical observations of equatorial plasma bubbles. Geophys Res Lett 30:1766. doi:10.1029/2003GL017301

Kil H, Su S-Y, Paxton LJ, Wolven BC, Zhang Y, Morrison D, Yeh HC (2004) Coincident equatorial bubble detection by TIMED/GUVI and ROCSAT-1. Geophys Res Lett 31:L03809. doi:10.1029/2003GL018696

Lühr H, Xiong C, Park J, Rauberg J (2014) Systematic study of intermediate-scale structures of equatorial plasma irregularities in the ionosphere based on CHAMP observations. Front Phys 2:15. doi:10.3389/fphy.2014.00015

Ossakow SL (1981) Spread F theories—a review. J Atmos Solar Terr Phys 43:437–452

Xiong *et al. Earth, Planets and Space* (2016) 68:121

Page 12 of 12

Ott E (1978) Theory of Rayleigh-Taylor bubbles in the equatorial ionosphere. J Geophys Res 83(A5):2066–2070. doi:10.1029/JA083iA05p02066

Park J, Lühr H, Noja M (2015a) Three-dimensional morphology of equatorial plasma bubbles deduced from measurements onboard CHAMP. Ann Geophys 33:129–135. doi:10.5194/angeo-33-129-2015

Park J, Stolle C, Xiong C, Lühr H, Pfaff RF, Buchert S, Martinis CR (2015b) A dayside plasma depletion observed at midlatitudes during quiet geomagnetic conditions. Geophys Res Lett 42:967–974. doi:10.1002/2014GL062655

Retterer JM (2010) Forecasting low-latitude radio scintillation with 3-D ionospheric plume models: 1. Plume model. J Geophys Res 115:A03306. doi:10.1029/2008JA013839

Richmond AD (1995) Ionospheric electrodynamics using Magnetic Apex Coordinates. J Geomagn Geoelectr 47:191–212

Singh S, Johnson FS, Power RA (1997) Gravity wave seeding of equatorial plasma bubbles. J Geophys Res 102(A4):7399–7410. doi:10.1029/96JA03998

Stolle C, Lühr H, Rother M, Balasis G (2006) Magnetic signatures of equatorial spread F as observed by the CHAMP satellite. J Geophys Res 111:A02304. doi:10.1029/2005JA011184

Stolle C, Lühr H, Fejer BG (2008) Relation between the occurrence rate of ESF and the equatorial vertical plasma drift velocity at sunset derived from global observations. Ann Geophys 26:3979–3988. doi:10.5194/angeo-26-3979-2008

Su S-Y, Yeh HC, Heelis RA (2001) ROCSAT 1 ionospheric plasma and electrodynamics instrument observations of equatorial spread F: an early transitional scale result. J Geophys Res 106(A12):29153–29159. doi:10.1029/2001JA900109

Su S-Y, Liu CH, Ho HH, Chao CK (2006) Distribution characteristics of topside ionospheric density irregularities: equatorial versus midlatitude regions. J Geophys Res 111:A06305. doi:10.1029/2005JA011330

Sultan PJ (1996) Linear theory and modeling of the Rayleigh-Taylor instability leading to the occurrence of equatorial spread *F*. J Geophys Res 101(A12):26875–26891. doi:10.1029/96JA00682

Thébault E et al (2015) International geomagnetic reference field: the 12th generation. Earth Planets Space 67:79. doi:10.1186/s40623-015-0228-9

Tsunoda RT (1980) Magnetic-field-aligned characteristics of plasma bubbles in the nighttime equatorial ionosphere. J Atmos Terr Phys 42:743–752. doi:10.1016/0021-9169(80)90057-4

Xiong C, Park J, Lühr H, Stolle C, Ma SY (2010) Comparing plasma bubble occurrence rates at CHAMP and GRACE altitudes during high and low solar activity. Ann Geophys 28:1647–1658. doi:10.5194/angeo-28-1647-2010

Xiong C, Lühr H, Ma SY, Stolle C, Fejer BG (2012) Features of highly structured equatorial plasma irregularities deduced from CHAMP observations. Ann Geophys 30:1259–1269. doi:10.5194/angeo-30-1259-2012

Yokoyama T, Su S-Y, Fukao S (2007) Plasma blobs and irregularities concurrently observed by ROCSAT-1 and Equatorial Atmosphere Radar. J Geophys Res 112:A05311. doi:10.1029/2006JA012044

Yokoyama T, Shinagawa H, Jin H (2015) Nonlinear growth, bifurcation and pinching of equatorial plasma bubble simulated by three-dimensional high-resolution bubble model. J Geophys Res Space Phys 119:10474–10482. doi:10.1002/2014JA020708

Zargham S, Seyler CE (1989) Collisional and inertial dynamics of the ionospheric interchange instability. J Geophys Res 94(A7):9009–9027. doi:10.1029/JA094iA07p09009